Earth Planets Space, **51**, 833–844, 1999

Dynamics of Neutral Wind in the polar region observed with two Fabry-Perot Interferometers

M. Ishii[1], S. Oyama[2], S. Nozawa[2], R. Fujii[2], E. Sagawa[1], S. Watari[1], and H. Shinagawa[2]

[1]*Communications Research Laboratory, Ministry of Posts and Telecommunications, Koganei, Tokyo 184-8795, Japan*
[2]*Solar-Terrestrial Environmental Laboratory, Nagoya University, Chikusa-ku, Nagoya 464-8601, Japan*

(Received August 10, 1998; Revised June 28, 1999; Accepted July 7, 1999)

Optical observations were made at Ramfjord, Norway from January 10 to February 14, 1997. Two types of Fabry-Perot interferometers (FPIs), Doppler-imaging and scanning, were installed at the EISCAT radar site and were used to acquire data simultaneously with radio instruments. Both FPIs can observe emissions of two different wavelengths simultaneously. We can estimate the horizontal and vertical wind in different emission layers simultaneously with high time-resolution ($\sim$1 min). The observations on February 8 and 9, 1997, show some notable characteristics: (1) large-scale perturbations ($\approx \pm$150 m/s) are observed in the upper thermospheric wind. They seem to begin 30 min after the onset of a magnetic substorm and to stop when the next substorm begins. (2) Clear wave-like structures are found in the horizontal wind variations. Some of them can be seen over the entire sky, and one of them is found in a restricted regions. (3) A clear wave-like structure is also found in the vertical wind in the upper thermosphere. A similar structure can be seen in the lower thermosphere, but these structures are not always in phase. This phases difference starts at the same time that horizontal winds between the two layer has their phase difference. (4) The relation between the vertical wind and the divergence of horizontal wind seems to change with time. The correlation coefficient between them changes one-hours before and on-time of a substorm on-set. This sign of the coefficient is negative in most of the time, with considering about time-lag. It means the vertical morion is caused by divergent flow of horizontal wind.

1. Introduction

The Earth receives two types of energy from the sun: radiation and the MHD energy associated with the solar wind. The latter energy is deposited in the ionosphere with Joule heating and particle heating in the polar ionosphere. These two heating systems according to field-aligned current are the last processes of solar energy deposition to the ionosphere. The neutral particles are accelerated and heated in this process, which is one of the main parts of thermosphere-ionosphere coupling. To evaluate the deposition of solar energy, it is important that we understand the relations between the field-aligned current, ion-neutral heating, and vertical wind.

Many theoretical studies of ion and electron heating by field-aligned current/particle precipitation have been published (e.g., Rees and Walker, 1968; Rees *et al.*, 1983). Rees and Walker (1968), for example, investigated the heating of ions and electrons by electric fields associated with the auroral electrojets. Model calculations for neutral heating were also executed (Roble and Rees, 1977; Fuller-Rowell *et al.*, 1991). Fuller-Rowell *et al.* (1991) estimated the effect of Joule heating in the polar thermosphere by using the UCL-Sheffield coupled model, and Walterscheid *et al.* (1985) estimated the vertical wind by using a local model.

Ion and neutral heating can be observed by radar (e.g., Kosch and Nielsen, 1995). This radar can accurately observe the energy flux of auroral particles as well as the ion and electron densities at any height, but some assumptions must be made if the net neutral wind velocity is to be estimated from radar observations.

Optical observations using interferometers provide information useful for estimating the wind velocity and temperatures in neutral dynamics. In particular, the neutral wind in the vertical direction that heating causes near an aurora has become the focus of recent studies (Rees *et al.*, 1984; Crickmore *et al.*, 1991; Aruliah and Rees, 1995; Conde and Dyson, 1995; Price *et al.*, 1995; Smith and Hernandez, 1995). Rees *et al.* (1984) reported that the vertical winds over 50 m/s were observed in the polar F-region during substorm recovery phase. Price *et al.* (1995) observed two different wavelength emission simultaneously with scanning Fabry-Perot interferometer (FPI). From these results they deduce a schematic model of vertical wind structure near aurora.

Simultaneous observations of radar and optical instruments are important to estimate the energy input and output, and many coordinate observations have been attempted (e.g., Hays *et al.*, 1970; Hernandez *et al.*, 1975; Wickwar *et al.*, 1984; Frey *et al.*, 1996; Haerendel *et al.*, 1996). In January and February of 1997, the EISCAT-FPI campaign was conducted. Two FPIs were installed at Ramfjord, Norway, and were used to make observations at the same time when the EISCAT-KST radar was operating. The main purpose of this campaign was to estimate the neutral wind using the two different techniques. This campaign also provided a good

opportunity to investigate the neutral-ion coupling process.

The key point of this campaign was that two kinds of FPIs, Doppler-imaging FPI and scanning FPI, were available simultaneously. Doppler-imaging FPI observation can be expected to estimate horizontal wind distribution with high time resolution. On the other hand, scanning FPI observation has the advantage of vertical wind estimation. Simultaneous observations with both of them are very important for compensating their respective disadvantages.

Other kinds of instruments were also used in this campaign (e.g., an all-sky imager, photometers, IS radar, MF radar, and magnetometers), and the data from those instruments have contributed to our understanding of the neutral-ion coupling. This paper discusses the three-dimensional neutral wind dynamics revealed in two case studies. It is important to analyze wind variation in the whole-sky, however, when auroral activity is relatively high and aurora has localized structures such as the present cases, analysis of averaged variation is not enough to explain the dynamics. In this paper, at first, spatially averaged wind variation obtained by VAD method will be discussed and after some small scale structure (e.g., local variation and divergence of horizontal wind) will be discussed.

2. Experimental Methods

The FPI observations for the EISCAT-FPI campaign were made between January 10 and February 14, 1997, at the EISCAT transmitter site (69.58°N, 19.22°E). The telescope for the scanning FPI had a narrow field of view (1.4 deg) and the observing direction (determined by mirrors in front of the telescope) could be scanned by motor-control. The all-sky FPI on the other hand, had a fish-eye view encompassing 140 deg. Details of the FPI instruments are described in Ishii *et al.* (1997). Each FPI used a dichroic mirror to measure two wavelengths simultaneously, and the channels mainly used in this campaign were those at 557.7-nm and 630.0-nm. The field of view of the scanning FPI was along the geomagnetic field (elevation: 77.54 deg, azimuth: 182.57 deg from North to East) when the EISCAT radar was operating and was vertical (elevation: 90.00 deg) when the radar was not operating. This paper deals with two case studies; Case 1 on Feb. 8 with simultaneous radar observations and Case 2 on Feb. 9 without radar observations. Vertical wind was also observed with scanning FPI in Case 2.

The heights of the 557.7-nm and 630.0-nm emission layers are generally thought to be about 110 km and 250 km, respectively (Sahai *et al.*, 1990; Mende *et al.*, 1993; Shepherd *et al.*, 1995), but Vallance Jones *et al.* (1991) reported that the peak height of 557.7-nm emission is about 125 km. Reflecting the uncertainty of the precise height of measurement, we shall refer to the 630.0-nm measurements as upper thermospheric winds and to the 557.7-nm measurements as lower thermospheric winds. Figure 1 is a diagram of observations in this campaign. The Doppler-imaging FPI observation made it possible for us to infer two-dimensional distributions of neutral wind velocity. However the observational regions and periods are restricted. For example, the wind structure could be inferred with high time resolution only at the emission layers and correspondent regions of fringes during night time.

The count rates of the 557.7-nm and 630.0-nm emissions were enhanced by a Photon Counting Imager (PCI, Hamamatsu V5102UHX (S-20/S-25)) and were measured by normal CCD cameras with a pixel count of 512 by 480 with output of 30 images every second. Output images from CCD cameras were integrated by an image processor for gaining a high S/N ratio. The integration time was 60 sec (integrating 1800 images). In this campaign three-order (A-ch) and four-order (B-ch) of fringes were observed in each instrument. The most inner fringe is used for analysis. The zenith angle of the most inner fringe corresponds to 15 deg in the Doppler Imaging FPI.

Calibration fringes were obtained with two kinds of He-Ne lasers; one with a peak wavelength of 632.7 nm for the A channel (630.0 nm) and the other with a peak wavelength of 543.5 nm for the B channel (557.7 nm). The fringe center variation due to etalon gap drift during one night was negligibly small.

We had implemented a temperature control for the etalon chamber, but there was still some etalon gap drift caused by temperature variations. The drift could be deduced from laser calibration data obtained every 3 hours and the temporal variation of averaged radii of fringes. In 12 hours the radii of most inner fringes decreased linearly by about 6 pixels. This total drift corresponds to 300 m/s of wind velocity.

Each fringe observed by the scanning FPI was integrated around the determined center and the fringe radius was measured by fitting Gaussian for each peak in the cross section. Two-hour averages of the radii of fringes observed by the scanning FPI were calculated and used as a baseline for reducing the effect of etalon gap drift. In addition a running average with 10-min window were used for analyzing the scanning FPI data for reducing high-frequency noise.

The analysis of Doppler Imaging FPI data were executed as a following sequences: 1) Each fringe was divided into 24 sectors with 15 degree azimuthal separations. 2) each fringe radius was determined by fitting a Gaussian function to each peak found in the cross section. 3) correct distortions of fringes using laser calibration data as a standard. 4) 2-hour average of peak position is calculated in each direction. 5) View aligned velocity was calculated using 2-hour average as a baseline. 6) The zonal and meridional component of wind velocity is deduced using VAD method. In this sequence view aligned velocity is transferred to horizontal velocity.

These operation makes difficult to discuss absolute value of wind velocities. In this paper small scale temporal variation ($\leq$2 hours) will be mainly discussed because of the restricted baseline determination.

We used the "VAD (velocity-azimuth display) method" (Sato, 1988) to estimate the zonal and meridional components of the dominant wind in the observing area from the results of Doppler-imaging FPI. When wind components are plotted as a continuous function of azimuthal angle, the horizontal component is indicated by the amplitude and the phase of the sinusoid. Then the zonal and meridional components are determined by using a least-squares method which is used to fit a sinusoidal curve to the variation of the horizontal wind component. The uniformity of horizontal wind in the observing area is assumed in this method.

Here the influence of etalon gap drift and vertical wind in the deduced horizontal wind with VAD method will be

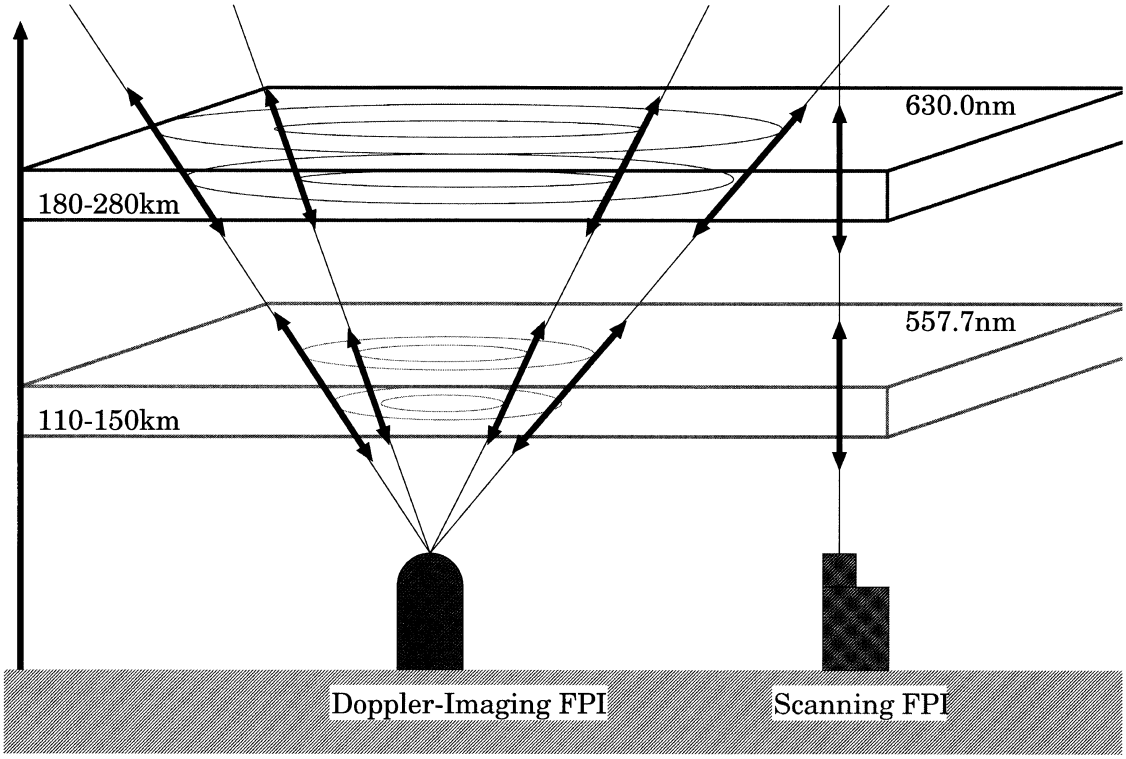

Fig. 1. Diagram of the observations in this campaign. The Doppler-imaging FPI had a wide field of view (140 deg) and could be used to investigate the distribution of horizontal wind velocities. The scanning FPI had a narrow field of view (1.4 deg) and could observe any point in the sky by using two mirrors. It was used for investigating the magnetic-field-aligned wind and the vertical wind. Each instrument can observe emissions at two wavelengths simultaneously (e.g. 557.7-nm and 630.0-nm), which means that wind velocity distributions at two heights could be inferred.

discussed. Firstly we discuss a case that all peaks in 24-directions have the influence equally. In this case a sinusoidal wave has offset and amplitude is not modulated by etalon gap drift and vertical wind. If the temporal variation of the etalon gap drift is not linear, it makes influence to the wind in the sequence 5) shown above. However, also in this case the influence was shown in offset, and not in amplitude, because parallelism of etalon gap keeps well and drift will be equally shown in 24-direction. Secondary we discuss the case that there are some effects of drifts and vertical wind in one or several points in 24-directions. In this case, the amplitude of fitting sinusoidal wind curve has some influence. However, in this case the fitting condition becomes poor and the standard deviation will increase. It is possible to deduce the effect of etalon gap drift/vertical wind on the hosizontal wind.

It is difficult to assume uniform wind systems in the polar thermosphere, especially in magnetic active period. On the beginning we estimate horizontal wind distribution in 24 direction. In some periods (e.g., 21:30–24:30 LT; 26:00–29:00 LT on Feb. 08, 1997) the wind distribution shows quite high uniformity. From this result we think it is worth calculating the zonal and meridional component of horizontal wind with VAD method. In addition we calculate standard deviation of the residual of the data-fitted model for an indication of non-uniformity.

A sensitive all-sky imager was used for observing the relative intensity and features of the aurora. The object lens of this imager was a fish-eye lens (Nikon, 8 mm F2.8) with a 180-deg. field of view. A cooled CCD made by Photometrics was used as a detector of the imager whose pixel number was 1024 by 1024. In this campaign the images were binned to 512 by 512. The integration time was 30 sec and each image was taken in every 5 min.

3. Results

3.1 Case 1: Feb. 08, 1997

The top and second panels in Fig. 2 show the zonal and meridional components inferred from the Doppler-imaging FPI data gathered on Feb. 08, 1997. Red and green lines respectively show the wind variations at the higher (deduced from 630.0-nm emission) and the lower (deduced from 557.7-nm emission) thermosphere. The third panel shows the standard deviation of the wind in VAD mehod. Having fitted a uniform wind, with a sinusoidal azimuthal variation, we calculated the residual of the data-fitted model, as a function of azimuth. The standard deviation of this residual was used as an indication of non-uniformity. The error of peak position determination in each direction can be estimated as $\sim$10 m/s from the results of Nakajima *et al.* (1995). (The error of absolute value becomes larger than that because of poor determination of baseline.) When the standard deviation is $\sim$20 m/s, the wind distribution can be well-estimated as uniform.

This case can be divided into five parts for the differences of wind behavior. In the first period, before 19:00 LT, the direction of the wind is toward Northwest and the power is decreasing. It is worth noting that the standard deviation

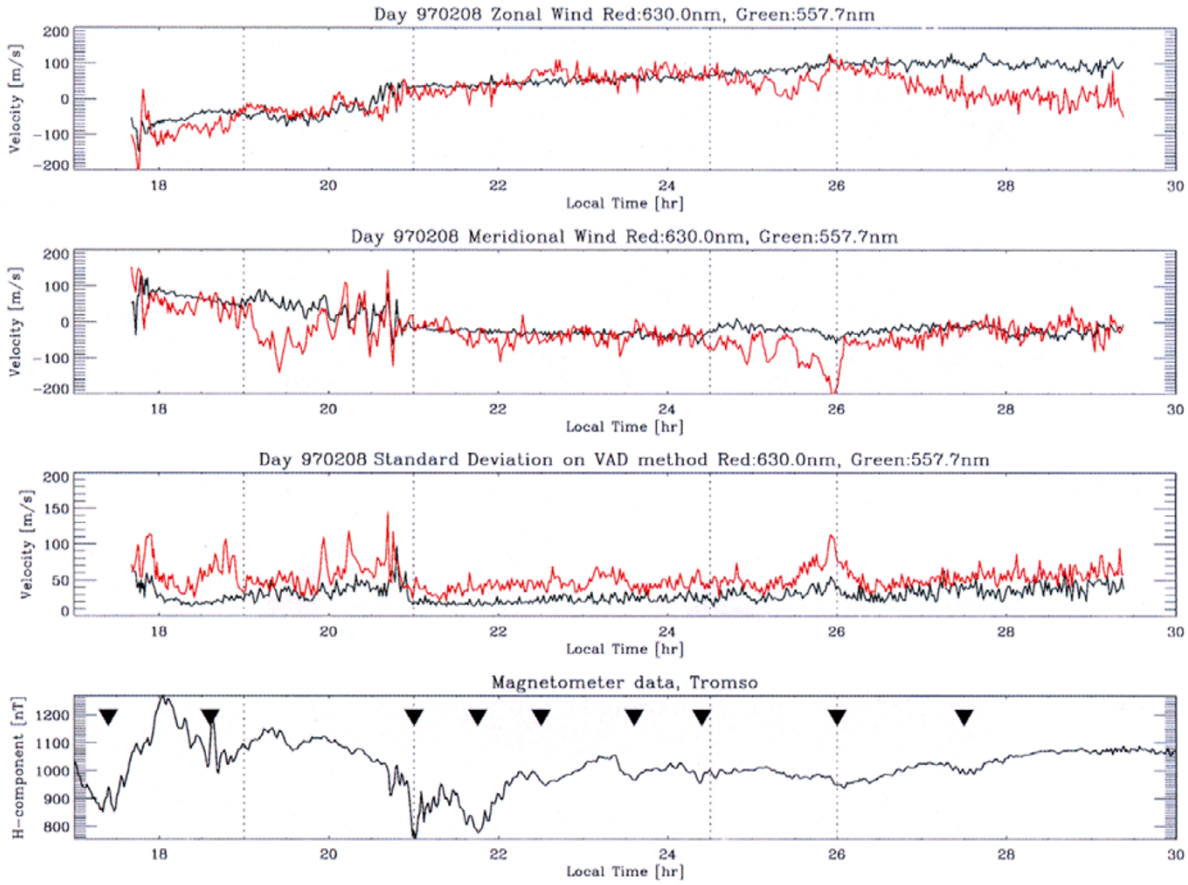

Fig. 2. Temporal variation of horizontal wind velocity observed on Feb. 08, 1997 (top two panels). Green and red lines in each panel respectively show wind velocities deduced from the 557.7-nm and 630.0-nm emissions. The third panel shows standard deviation of wind velocity from the assumed uniform wind. The lower panel shows the H-component of ground-based magnetometer data gathered in Tromsø, about 10 km west of Ramfjord. The offset is 10,000 nT. Filled marks show the time of substorm on-set.

increasing with a magnetic substorm occuring in the latter of this period (after 18:20 LT). In the second period, from 19:00 to 21:00 LT, the meridional component of the upper thermospheric wind has large perturbations which become 150 m/s in absolute value. In the zonal component, on the other hand, there are some phase differences between the lower and upper thermospheric winds, but the absolute values of the two winds are similar. The standard deviation in the latter in this period becomes poor, which shows the wind distribution has some divergence and it is difficult to consideer as a uniform wind. In the third period (21:00–24:30 LT), the general trend of wind velocity is almost the same in the lower and upper thermosphere; however, the small-scale perturbation in the upper thermosphere is larger than that in the lower one. In the fourth period (24:30–26:00 LT), the upper thermospheric wind shows a clear wave-like structure. Figure 3 shows hodograph in this period. It can be seen a clock-wise polarization in the wind in 24:55–25:25 LT. The standard deviation between 25:25–26:15 LT become high, so the assumption of uniform wind is thought to be poor in this period. After 26:00 LT, the difference between the variations of the upper and lower thermospheric winds is greater in the zonal than in the meridional ones. In the zonal component, the upper thermospheric wind decreases slowly. There is also a clear change in the lower thermospheric wind at 26:00 LT. At this time the zonal component stopped increasing and becomes nearly constant. The standard deviation increases in the first, second and the latter of fourth periods. It should be noted that these results show relative variation in small scale. For example, in the third period the value of wind velocity is quite similar, but the absolute value can vary by the determination of baselines. The result represents that a uniform winds exist stably in this period.

The bottom panel shows the H-component of the magnetic field observed at Tromso, about 10-km west of the EISCAT radar site. The offset of the H-component is 10,000 nT. This magnetometer data shows that fairly large substorms were observed in this period, and some of them occurred before the FPI observation started. The Kp indices in those periods are 4− (19:00–22:00 LT), and 2+ (22:00–30:00 LT).

Substorm onsets occurred at the time marked in the lower panel during these observations, and the significant feature emerging from the comparison of wind variation and geomagnetic variation is that a strong substorm accelerate neutral wind gradually. This is especially evident from 19:00 to 21:00 LT, when the meridional component of the wind shows large-amplitude perturbations but the magnetic field does not. Before this wind perturbation started, there were at least two substorms and another wind perturbation started just after the recover phase of the latter one. When the next

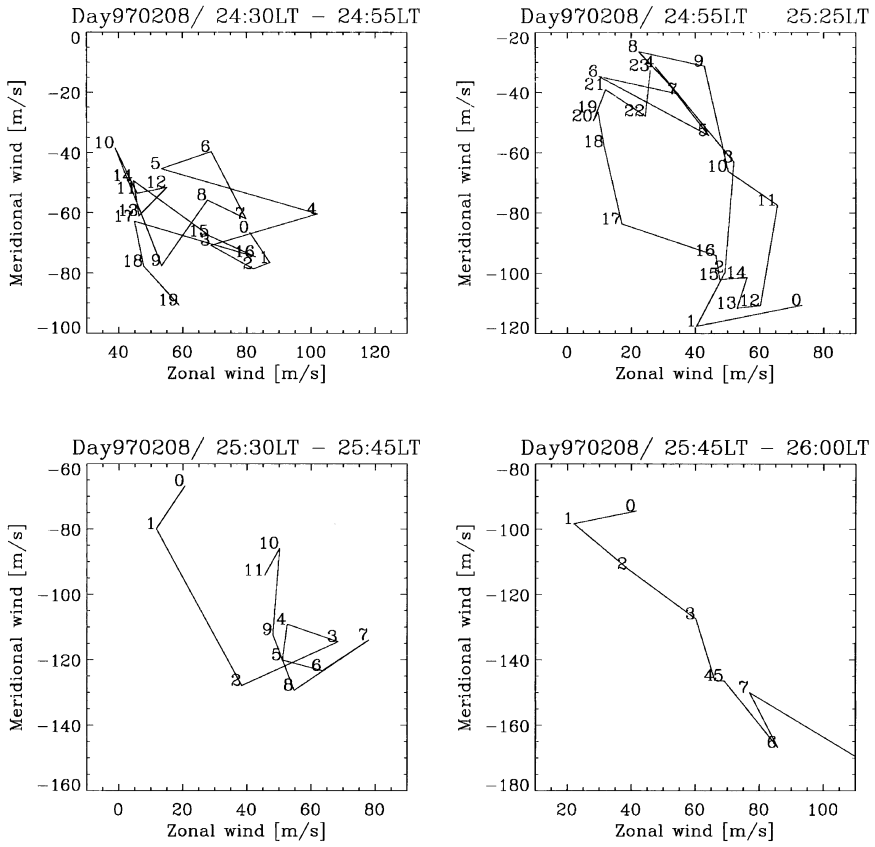

Fig. 3. Polarization of upper thermospheric wind observed between 24:30–26:00 LT.

substorm onset occurred (≈20:40 LT), this perturbation in neutral wind also disappeared.

A similar phenomena occurred at 26:00 LT. There were some small-scale magnetic field perturbations before the neutral wind oscillation started at 24:00 LT, and when the oscillation stopped another small-scale magnetic substorm began at 26:00 LT. The variation in the H-component is not clear, but the auroral image data in Fig. 4 shows that there was some auroral activity at that time. Figure 4 shows the zonal and meridional distribution of auroral luminosity obtained by an all-sky imager. Bright auroras appeared at the beginning of the optical observations (before 18:00 LT) and again around 21:00 LT. In addition, a relatively weak aurora can be seen at 26:00 LT. The brightest aurora appeared at 21:00 LT, which corresponds to the onset of the magnetic substorm, and this is the time that neutral wind disappeared. The single arc aurora appeared at 26:00 LT located on east-west, and the time corresponds to the time when the upper thermospheric winds oscillation disappeared. The all-sky image shows that pulsating auroras appeared after the arc disappeared. The luminosity at 630.0 nm obtained with a photometer increased from 20 kR to 80 kR at 26:00 LT and decreased to several kilorayleighs after that.

3.2 Case 2: Feb. 09, 1997

The vertical wind was observed by the scanning FPI, on the other hand the Doppler-imaging FPI data could not be obtained after 23:30 LT because of trouble in the image processor for the Doppler-imaging FPI.

Figure 5 shows the magnetometer data and the horizontal wind estimated from the Doppler-imaging FPI. The format is the same as that in Fig. 2. Comparing the upper and lower thermospheric wind variations, we can see that the zonal components of both winds are quite similar. However, a difference of wind distributions in the two emission layer can be inferred from the standard deviation in this period. In the higher altitude, the standard deviation often exceeds 100 m/s, on the other hand, in the lower altitude, it keeps about 50 m/s. This means that the wind distribution does not become often uniform in the higher altitude, and the uniformity keeps well in the lower altitude. Comparing the zonal and meridional components at each altitude, we find that at both altitudes the variation in the meridional component is larger than that in the zonal component. Before 20:00 LT, the lower thermospheric zonal wind is oscillating between −50 m/s and zero and the upper thermospheric zonal one is oscillating between −100 m/s and zero. At the meridional component, the lower and upper thermospheric wind have quite similar variations except around 19:00 LT. From 18:40 to 19:20 LT, for example, the amplitude of the meridional component in the upper wind was 100 m/s. From 20:00 to 21:40 LT, the difference of the zonal wind between the lower and the upper thermosphere is almost zero. However, the meridional component of the upper thermosphere becomes −180 m/s southward. During the next period, 21:40–22:00 LT, some rotational structure in the upper thermospheric wind can be seen. The rotational period is rather short, ≈10 min, and

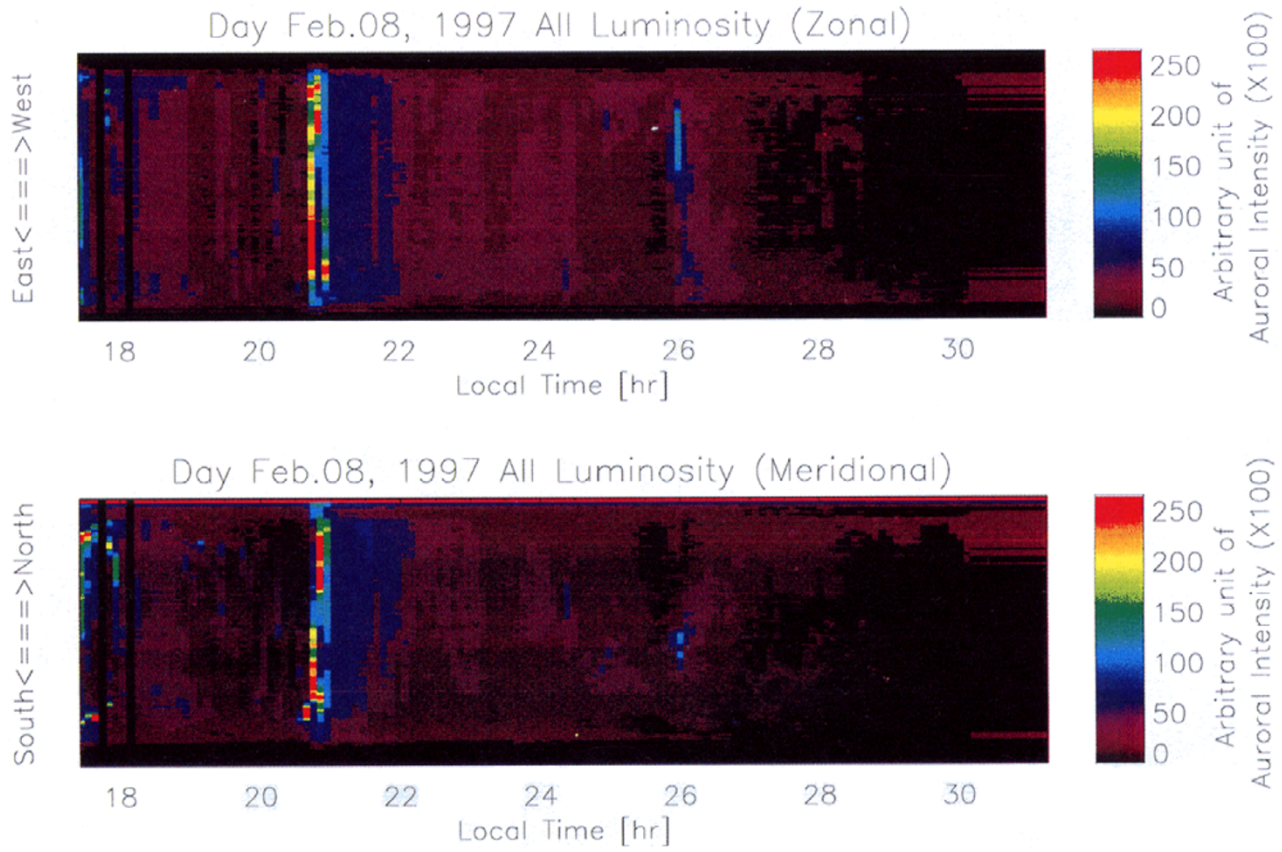

Fig. 4. The zonal and meridional distribution of relative (uncalibrated) auroral luminosity obtained by an all-sky imager on Feb. 08, 1997. No optical filters were used, and the field of view is ≈180 deg.

the horizontal wind direction rotates twice anti-clockwise. After 22:00 LT, the difference between the lower and upper thermospheric wind decreases. The standard deviations (the third panel) shows relatively high, especially 19:30–20:00, 21:00–21:15 and after 22:30.

The bottom panel shows that a large magnetic substorm onset occurred at 21:10 LT (marked time in the panel). The Kp indices in those periods are 4 (16:00–19:00 LT), 5+ (19:00–22:00 LT), and 4 (22:00–25:00 LT). Comparison of the wind velocity and magnetic field data shows that there are gradual response of magnetic activity in the neutral wind after the onset of a strong magnetic substorm shown at 21:10. The acceleration to the Southeast in the horizontal wind starts at 21:30 and continue for about one hour.

Figure 6 shows the vertical wind estimated from the scanning FPI and shows the divergence of horizontal wind estimated from the Doppler-imaging FPI. The positive divergence implies a net outflow, or source of matter, and the negative divergence implies a net inflow, or sink of matter. Running-average window for smoothing the vertical wind variations is 10 min. The same magnetometer data shown in Fig. 5 is shown again for reference in the bottom panel.

The upper panel in Fig. 6 shows that the vertical wind velocities in the upper and lower thermosphere change similarly until 19:45 LT. The vertical wind accelerates downward until 18:30 LT and then accelerates upward. After 19:45 LT the upper and the lower thermospheric vertical winds have different temporal variations: The variation of the upper thermospheric wind has a wave-like structure whose amplitude is ≈40 m/s and period is ≈1 hour. In the lower thermosphere the wind has a wave-like structure but the amplitude is half as large as that in the upper thermospheric wind. These variations are also not in phase with each other. The wind variations in the two layers start to differ at 19:45 LT, about 1:20 before the onset of the magnetic substorm. This time is almost the same time that the meridional components of the horizontal wind begin to differ (Fig. 5, second panel from the top). The data shown in Fig. 6 thus reveals that the vertical winds also start to differ 1:20 before the onset of the magnetic substorm.

The relation between the averaged vertical wind and the divergence of horizontal wind changes with local time. Figure 7 shows the results of cross-correlation between the vertical and the divergence of horizontal wind with considering time delay. The correlation were calculated in each one-hour window. The horizontal axis presents the observing time of Doppler-Imaging FPI in which the window was set ±30 min. The one-hour window was set in the vertical wind, too. Time delay of cross-correlation is set ±30 min. The vertical axis shows the time delay.

For both wavelength, phase lag between the vertical wind and the divergence of horizontal wind varies with local time. In 557.7 nm (the upper panel) there are strong positive correlation around 10 min lag and strong negative correlation

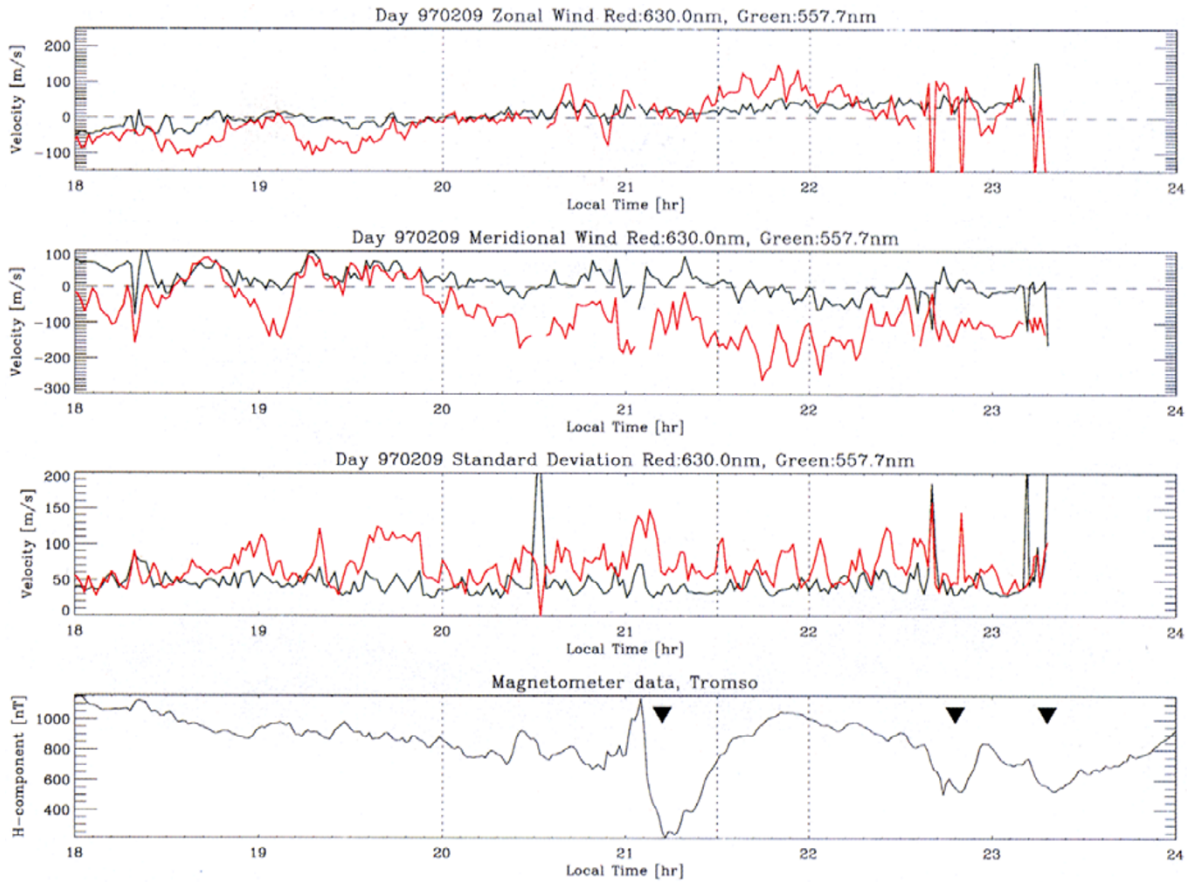

Fig. 5. Temporal variation of horizontal wind velocity observed on Feb. 09, 1997. The format is the same as that of Fig. 2.

around 30 min lead between 19:00–19:30 LT. From 19:30 to 21:30 LT there are strong negative correlation in 0 min lag and strong positive correlation in 20 min lag. In 630.0 nm, there are fairly strong correlation in 0 min lag, and strong positive in 30 min lag between 19:00 and 20:30 LT. There are strong negative correlation in 10 min lag from 20:30 to 21:10 LT. Strong positive correlation is around 15 min lag from 21:30 to 22:00 LT.

Figure 8 shows the variation in auroral luminosity during Case 2. The format is the same as that in Fig. 4. This figure shows that bright auroras appeared in the whole sky at 21:10 LT and at 22:45 LT and that there were fairly bright auroras in the southwestern sky from 18:00 to 23:00 LT. They often moved until the first break up (21:10 LT) but become stable after that. The time of auroral break up is almost the same as that of the magnetic substorm onset, but at the time the temporal variation in the wind has no significant changes.

4. Discussion

Our results show very complicated wind variations in each layer. These complicated structures can be thought to be a result of the overlapping of some factors: (1) the global wind system, (2) large/medium-scale gravity waves propagating from distant regions, and (3) gravity waves generated by local heating. Our results shown here suggest the importance of interactions between global flows and gravity waves, and interactions between gravity waves. In addition, our results show difficulties to find the source of wind variation because more than two of factors give influence to the neutral dynamics in each case.

One of the most notable phenomena in the two cases is that some of magnetic substorm on-set correspond to gradual acceleration of neutral wind. In Case 1 there were two significant perturbations in wind velocity, from 19:00 to 20:45 LT and from 24:45 to 26:00 LT, and there were some substorm on-set before these wind perturbation occurs. In addition, there were magnetic activities after the perturbations had stopped. In the earlier event a large substorm began at 21:00 LT. In the later event a small magnetic variation and an auroral arc was observed (26:00 LT). In Case 2, the Kp indices were larger than those in Case 1 and the disturbances were also seen in the magnetometer data before on-set of the large substorm at 21:12 LT. Furthermore, the maximum meridional wind and large perturbations were observed after the on-set of the large substorm. These results show that the energy (or momentum) input by the large substorm caused the acceleration of wind.

Some previous work shows that the thermospheric wind accelerates associated with increasing auroral luminosity (Rees *et al.*, 1984; Frey *et al.*, 1996). Some other studies show that there are some strong winds several minutes before auroral breakup (e.g., Price *et al.*, 1995), but our results are notable in the following points; (1) the wind variation has a wave-like structure with high frequency (∼15 m/s es-

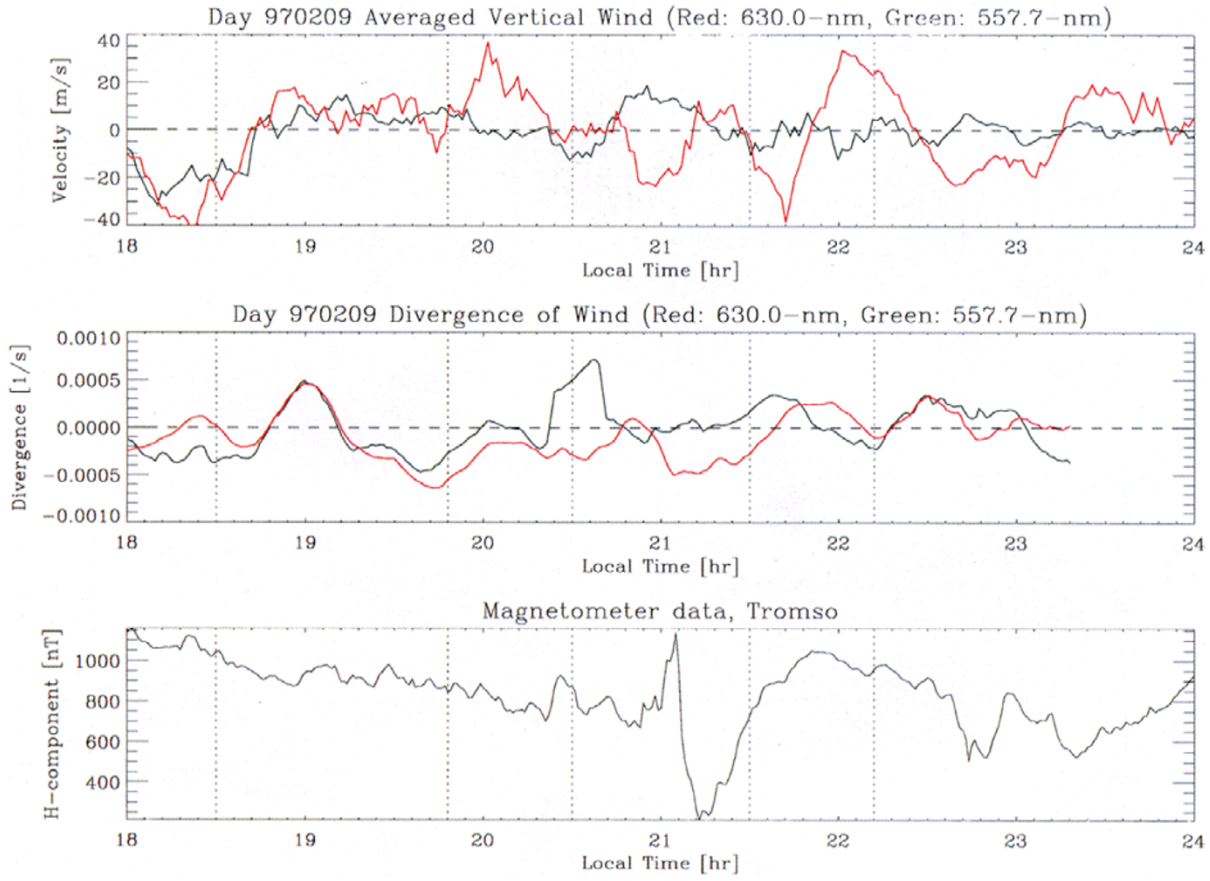

Fig. 6. Top panel: temporal variation of averaged vertical wind obtained by scanning FPI observation on Feb. 09, 1997. Middle panel: temporal variation of divergence of horizontal wind obtained by Doppler-imaging FPI. Lower panel: the same magnetometer data shown in the lower panel of Fig. 5.

pecially in the upper thermosphere), and (2) these large wind fluctuations stopped suddenly when a large substorm on-set occured. Conde and Smith (1998) also introduce an event in which thermospheric wind velocity decreases at the auroral breakup. They explained the phenomena by enhancement of wind in the opposite direction. But in our case it seems difficult to explain it in that way, because the wind stops so sharply.

One possibility of the reason why the large wind perturbation stopped suddenly (at 21:00 LT and 26:00 LT in Case 1) may be explained by some interactions between gravity waves propagating from distant regions and the wind system generated by local heating.

The uniformity of wind in the whole sky is assumed in Figs. 2 and 5. However, as some studies mentioned, the horizontal wind distribution cannot be assumed uniform in some cases. Conde and Smith (1998), for example, shows rotational and diverged distribution of horizontal wind in their examples. In our case, the standard deviation of residual between observed and uniform wind becomes sometimes high. At that time the uniformity of wind distribution is not a good assumption and some discussion will be needed about the spatial distribution of the wind. The significant perturbation of the upper thermospheric wind between 19:00 and 21:00 LT in Case 1 should be analyzed in more detail. Figure 9 shows the variation of wind velocity in 24 azimuthal directions for Case 1. The wind toward the observing point is positive. The lower panel shows the wind velocity in the area marked by a white line in the upper panel, an area in which meridional winds of large amplitude were seen in Fig. 2. The bottom line shows wind variation at the westward, and the top line shows that at southeast. These curves are shifted by 100 m/s. We can see some clearly wave-like variations in the lower panel of Fig. 9 (shown by the red line). The amplitude is 100–150 m/s and the period is about 15 min. The Brunt-Väisälä frequency in this layer is much dependent on the local time and solar activity, however, it will become 6–7 min in 200 km altitude and 11 min in 300 km altitude in the night time (Kelly, 1989). Thus it is possible to consider that the wave-like variation is gravity wave. This structure is localized in this direction; clear structures cannot be found in the opposite direction. These wave-like structures were measured for Southward from the observed point just before the onset of a magnetic substorm. Auroral movement at this time cannot be seen easily in Fig. 4 because of poor temporal resolution, but the lower panel shows that a bright aurora comes from South to North. This means that these wave-like structures disappear when the aurora becomes bright. So it is possible that the wind generated by local heating with aurora destroys the wave-like structure. Comparing with the event shown in 19:00–21:00 LT, the wave-like structure shown in 24:25–26:00 LT was observed in the whole sky. In this period

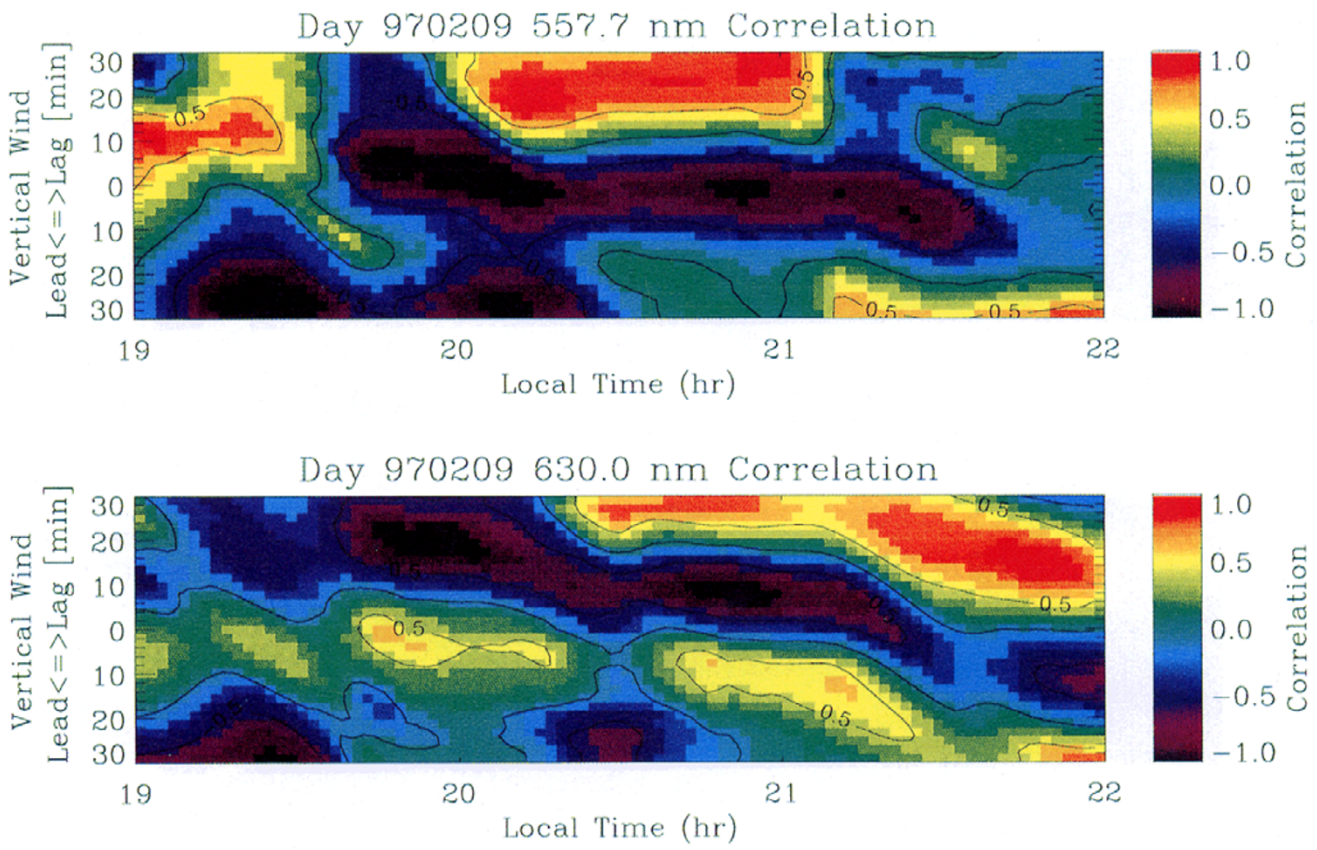

Fig. 7. Correlation between the vertical wind and the divergence of the horizontal wind observed on Feb. 9, 1997. The upper and lower panel shows the results of 557.7-nm and 630.0-nm, respectively. Correlation coefficient is calculated in 1-hour window. Horizontal axis show the central time of 1-hour window in horizontal wind observation. The time-lag between horizontal and vertical wind is also considered in this analysis. The vertical axis shows the time-lag of vertical wind observation from the observation time of horizontal wind.

the standard deviation increases in the latter of this period, but they are pretty small until 25:25 LT: so the assumption of uniform wind still works well. This wave-like structure has a polarization whose period is 25 min, rotation is clock-wise and the direction of major axis of the polarization is NW-SE. These parameters agree on condition shown in acorstic gravity waves.

Another possibility to explain this phenomena is the change of emission-layer height. The neutral wind dynamics based on radar-observation and chemical release studies are known to vary strongly as a function of altitude. We think this effects is much important for 557.7-nm analysis, but 630.0-nm analysis is not sensitive to the effect. The emission layer of 630.0-nm is generally wide (200–300 km; e.g., Banks *et al.*, 1974) and it is considered that the neutral wind deduced from FPI observations is an average of winds in the heights of emission layer with an emission profile as a weighting function (McCormac *et al.*, 1987). This emission profile is dependent on energies of precipitating particles, but averaged wind velocity does not sensitive to particle energy because averaging area is wide and horizontal wind profile in the area is relatively uniform. We prepare another study for comparison between the ion velocity estimated from EISCAT observation and our results averaged with estimated emission profile as a weighting function. The results shows that in Case 1, the averaged winds does not vary so much in the energy range from 0.5 keV to 30 keV.

The emission layer of 557.7nm has more serious problems. This emission layer is sharp and the peak emission height is under the influence of auroral particle energy. In addition, numerous rocket studies show that the auroral E-region winds undergo a strong rotation with altitude (e.g., Mikkelsen *et al.*, 1987; Larsen *et al.*, 1989; Larsen *et al.*, 1997). The examples of one of the strongest wind shear in these studies is shown in Larsen *et al.* (1997). The wind profile, observed during high magnetic activity on Feb. 12, 1994 (figure 3 in their paper), shows $\pm$200 m/s between 100 km and 150 km altitude which is considered as the range of a peak emission height of 557.7 nm. In addition the direction varies over 360 deg in this region. This is one of the most significant examples, and usually the wind shear is $\sim \pm$100 m/s but the rotation of wind direction is typical. Furthermore, the height of emission layer cannot be considered as uniform like Fig. 1; discrete bright auroral forms are likely to correspond to lower emission altitudes. So, at many times it is very difficult to interpret horizontal wind distribution deduced from 557.7 nm emission with no information of emission height. In our case, the averaged wind deduced from 557.7 nm is presented for instrument diagnostic purposes only.

We must accept that our results are always threatened by etalon gap drift. We cannot deny the possibility that the baseline varies over a shorter periods than laser sampling period

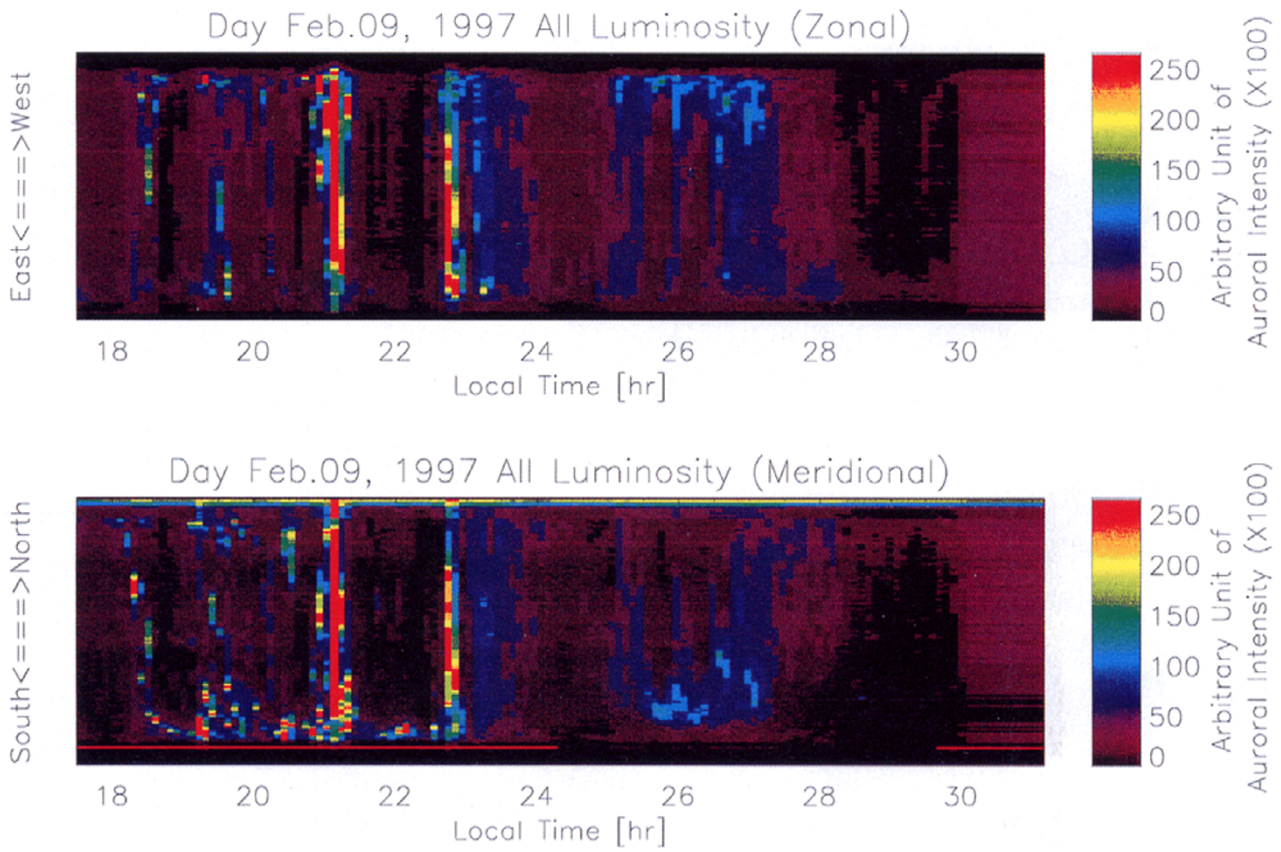

Fig. 8. The zonal and meridional distribution of relative auroral luminosity obtained on Feb. 09, 1997. The format is the same as that of Fig. 4.

(~3 hour). However, if the etalon gap drift is dominant in our results, both of wind deduced from 557.7 nm and 630.0 nm would vary in the same sense. For example, from 18:30 to 19:50 in Fig. 6, the variation of both winds are quite similar, and the effect of etalon gap drift can be suspected. But after 19:50, the two wind time series vary in anti-phase. The possibility that etalon drift modulated the derived wind velocities still remains, but we believe that it was not dominant in this period.

It is still difficult to determine zero velocity. The estimates most other experiments use are, (1) the average peak position from several opposing viewing directions, (2) the vertical peak position, (3) the peak position observed in cloudy nights, and (4) the average peak observed in long-term period. In using each baseline method, we are making certain assumptions about the winds in the thermosphere. Using (1) assumes that there is no horizontal divergence over the whole observing period. Using (2) assumes that the average vertical wind over the whole observing period is zero. For (3), it is assumed that the observing emission is well scattered by clouds particles and that the emission can be considered as summation of emission from the whole sky. For (4), it is assumed that the averaged wind does not deflect to a certain direction. We use (1) for Doppler-imaging FPI. As mentioned before, the zero divergence assumption will be wrong at some times. The departure of the observed wind field from uniformity is estimated as a standard deviation. (the third panel of Figs. 2 and 5). The zonal and meridional component has meaning only when these values are small. Our scanning FPI baseline is determined by (4), but very over a short period. We cannot avoid the possibility that this baseline has an offset.

Some possibilities can be found to explain why neutral wind perturbations do not correspond to the substorm on-set immediately. One is propagating gravity waves generated by auroral heating at other substorms. Another one is also gravity waves but generated locally. Because neutral wind in the upper thermosphere can be generated by auroral particles with small energy, considerable neutral wind can be observed even if there are not bright auroras in the region. And we must consider about the time lag for momentum and energy transfer from precipitating particle to neutral.

The relationship between the divergences of the horizontal wind and the vertical wind has been treated in some studies (Burnside *et al.*, 1981; Smith and Hernandez, 1995). Burnside *et al.* (1981) mentioned that if the rate of change of pressure at the level of the airglow emission is negligible, the following simple relation is obtained:

$$w = H\left(\frac{\partial u}{\partial x} + \frac{\partial v}{\partial y}\right), \tag{1}$$

where u, v, and w respectively mean the zonal, meridional, and vertical wind components. The constant of proportionality is H, the scale height of the layer in consideration. In this equation, Burnside *et al.* (1981) imply that this proportionality is positive; Smith and Hernandez (1995), however, found the proportionality to be negative and measured abso-

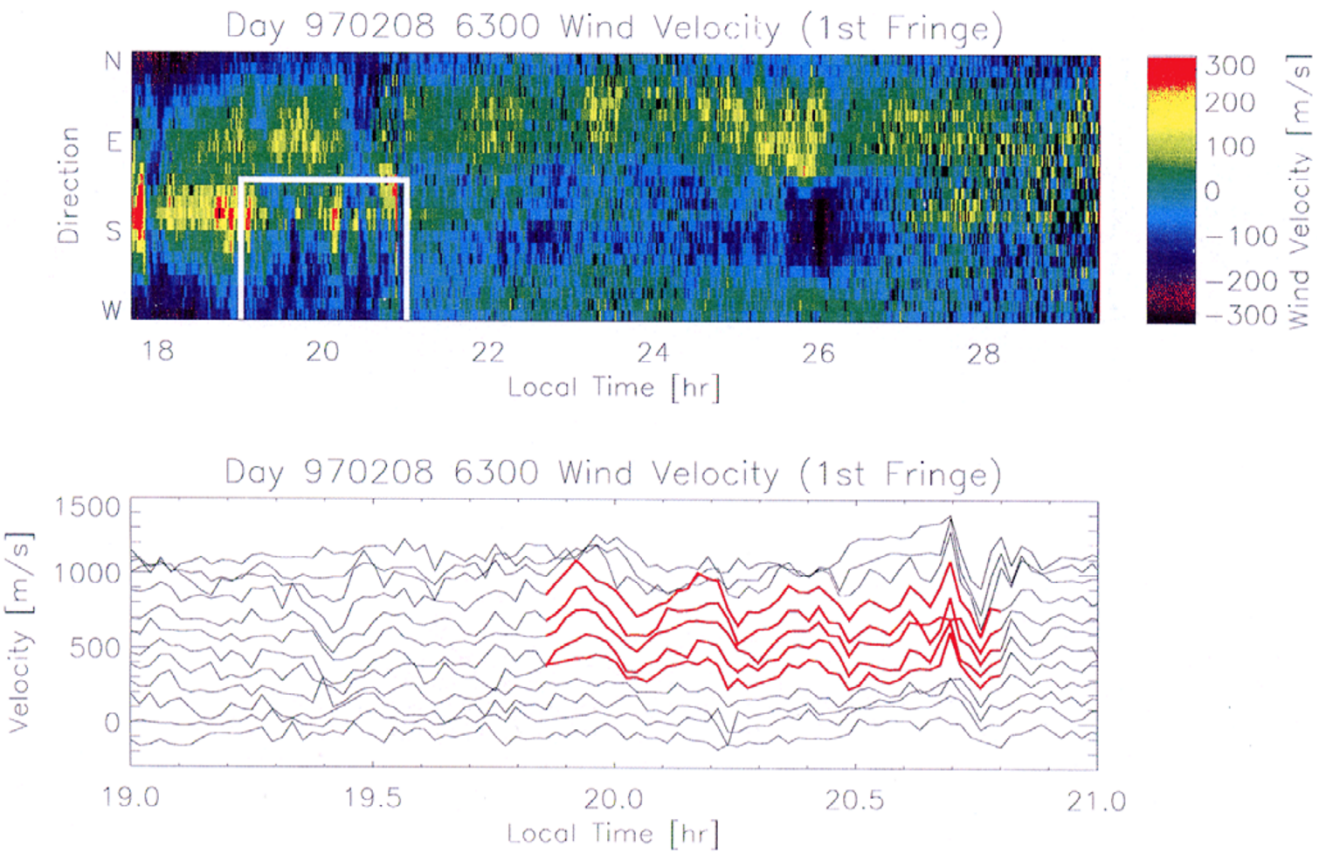

Fig. 9. Upper panel: temporal variation of wind velocity in 24 directions. The wind toward the observing point is positive. Lower panel: detailed temporal variation of horizontal wind in the area marked by a white line in the upper panel. Each baseline is shifted by 100 m/s for display.

lute values that were approximately double the scale heights at the altitude under consideration. They explained that this difference in sign comes from the difference of the system of the vertical wind. In the system imagined in Burnside *et al.* (1981) vertical motion is the origin of divergent flow. Smith and Hernandez (1995), on the other hand, suggested that the vertical motion is caused by divergent flow imposed by a driving force that acts horizontally, such as ion drag.

Burnside *et al.* (1981) adopted some assumptions to introduce Eq. (1), e.g., the rate of change of pressure at the level of the airglow emission is negligibly small. This assumption may not be able to adopted in our case because they are both trangent cases. It can be the reason why vertical wind variation delay from that of the divergence of horizontal wind. They examined for evaluating the characteristic time for pressure to change owing to vertical wind flow. The value τ_p ($= H/w$, equation (9) of their paper) can be estimated to ~20 min because vertical wind is about 40 m/s. It is consistent to the time lag between vertical wind and divergence of horizontal wind. The wind system shown during 19:30–21:30 LT in Fig. 7 can be explained that the vertical wind is caused by divergence flow, because (1) the vertical wind has time delay from divergence of horizontal wind, and (2) their correlation coefficient is negative.

The absolute values of the horizontal and vertical winds are consistent with those measured in many other studies. Kosch *et al.* (1997, 1999) show results obtained by a scanning FPI at Skibotn, 45-km southeast of Ramfjord, and our results are fairly consistent with theirs. Some detailed studies about these simultaneous observations will be published in the near future. Conde and Dyson (1995) show that the absolute value of the vertical wind velocity is less than 50 m/s in almost all of the 959 measurements. Aruliah and Rees (1995) and Smith and Hernandez (1995) also present similar values, and our results are consistent with theirs.

5. Concluding Remarks

Horizontal wind distribution and vertical wind data were obtained from two types of ground-based FPI instruments at Ramfjord, Norway. One of the advantages of these instruments is that emissions at two wavelengths can be observed simultaneously by using a dichroic mirror. Some notable observations made on Feb. 08 and 09, 1998, are the following:

- Large-scale perturbations ($\approx \pm 150$ m/s) are observed in the upper thermospheric wind. These perturbations correspond to the onset of magnetic substorms gradually.
- Clear wave-like structures are found in the horizontal wind variations. Some of them can be seen over the whole field of view, and one of them is found in a restricted region.
- A clear wave-like structure is found in the vertical wind in the upper thermosphere. A similar structure can be seen in the lower thermosphere, but the two structures

are not always in phase. This phase difference starts at the same time that horizontal winds in the two layer has their phase difference.

- The relation between the vertical wind and the divergence of horizontal wind changes with time. Considering about the time lag, the correlation coefficient between them is negative in most of the time. It means that the horizontal wind is the origin of the vertical wind.

Acknowledgments. We are indebted to the Director and staff of EISCAT for operating the facility and supplying the data. EISCAT is an international association supported by Finland (SA), France (CNRS), the Federal Republic of Germany (MPG), Japan (NIPR), Norway (NFR), Sweden (NFR) and the United Kingdom (PPARC). The data archives and processing have been made at STEL, Nagoya University. This study has been supported in part by the U.S.-Japan International Research Project to Observe the middle atmosphere, CRL, the Ministry of Posts and Telecommunications, and Grant 07044079 under the Monbusho International Scientific Research Program, the Ministry of Education, Japan.

References

Aruliah, A. L. and D. Rees, The trouble with thermospheric vertical winds: geomagnetic, seasonal and solar cycle dependence at high latitudes, *J. Atmos. Terr. Phys.*, **57**, 597–609, 1995.

Banks, P. M., C. R. Chappell, and A. F. Nagy, A new model for the interaction of auroral electrons with the atmosphere: spectral degradation, backscatter, optical emission, and ionization, *J. Geophys. Res.*, **79**, 1459–1470, 1974.

Burnside, R. G., F. A. Herrero, J. W. Meriwether, Jr., and J. C. G. Walker, Optical observations of thermospheric dynamics at Arecibo, *J. Geophys. Res.*, **86**, 5532–5540, 1981.

Conde, M. and P. L. Dyson, Thermospheric vertical winds above Mawson, Antarctica, *J. Atmos. Terr. Phys.*, **57**, 589–596, 1995.

Conde, M. and R. W. Smith, Spatial structure in the thermospheric horizontal wind above Poker Flat, Alaska, during solar minimum, *J. Geophys. Res.*, **103**, 9449–9471, 1998.

Crickmore, R. I., J. R. Dudeney, and A. S. Rodger, Vertical thermospheric winds at the equatorward edge of the auroral oval, *J. Atmos. Terr. Phys.*, **53**, 485–492, 1991.

Frey, H. U., G. Haerendel, D. Knudsen, S. Buchert, and O. H. Bauer, Optical and radar observations of the motion of auroral arcs, *J. Atmos. Terr. Phys.*, **58**, 57–69, 1996.

Fuller-Rowell, T. J., D. Rees, S. Quegan, and R. J. Moffett, Numerical simulations of the sub-auroral F-region trough, *J. Atmos. Terr. Phys.*, **53**, 529–540, 1991.

Haerendel, G., B. U. Olipitz, S. Buchert, E. Rieger, and C. La Hoz, Optical and radar observations of auroral arcs with emphasis on small-scale structures, *J. Atmos. Terr. Phys.*, **58**, 71–83, 1996.

Hays, P. B., A. F. Nagy, K. D. McWattiers, and J. V. Evans, Comparison of radar and optical temperature measurements in the F region, *J. Geophys. Res.*, **75**, 4881–4882, 1970.

Hernandez, G., T. E. VanZandt, V. L. Peterson, and J. P. Turtle, Comparison of optical and incoherent scatter measurements of nighttime exospheric temperature at the magnetic equator, *J. Geophys. Res.*, **80**, 3271–3274, 1975.

Ishii, M., S. Okano, E. Sagawa, S. Watari, H. Mori, I. Iwamoto, and Y. Murayama, Development of Fabry-Perot interferometers for airglow observations, *Proc. NIPR Symp. Upper Atmos. Phys.*, **10**, 97–108, 1997.

Kelly, M., The Earth's ionosphere, *Academic press*, 484 pp., 1989.

Kosch, M. J. and E. Nielsen, Coherent radar estimates of average high-latitude ionospheric Joule heating, *J. Geophys. Res.*, **100**, 12201–12215, 1995.

Kosch, M. J., A. Kohsiek, K. Schlegel, and T. Hagfors, A new Fabry-Perot interferometer experiment for neutral atmosphere studies in conjunction with the EISCAT incoherent-backscatter radar system, pp. 42, MPAE-T-010-97-20, 1997.

Kosch, M. J., A. Kohsiek, T. Hagfors, and K. Schlegel, Fabry-Perot interferometer measurements neutral atmospheric winds and temperatures near EISCAT—Initial results, *Ann. Geophys.*, 1999 (submitted).

Larsen, M. F., I. S. Mikkelsen, J. W. Meriwether, R. Niciejewski, and K. Vickery, Simultaneous observations of neutral winds and electric fields at spaced locations in the dawn auroral oval, *J. Geophys. Res.*, **94**, 17235–17243, 1989.

Larsen, M. F., A. B. Christensen, and C. D. Odom, observations of unstable atmospheric shear layers in the lower E region in the post-midnight auroral oval, *Geophys. Res. Lett.*, **24**, 1915–1918, 1997.

McCormac, F. G., T. L. Killeen, B. Nardi, and R. W. Smith, How close are ground-based Fabry-Perot thermospheric wind and temperature measurements to exospheric values? A simulation study, *Planet. Space Sci.*, **35**, 1255–1265, 1987.

Mende, S. B., G. R. Swenson, S. P. Geller, R. A. Vierech, E. Murad, and C. P. Pike, Limb view spectrum of the Earth's airglow, *J. Geophys. Res.*, **98**, 19117–19125, 1993.

Mikkelsen, M. F. Larsen, M. C. Kelley, J. Vickrey, E. Friis-Christensen, J. Meriwether, and P. Shih, Simultaneous measurements of the thermospheric wind profile at three separate positions in the dusk auroral oval, *J. Geophys. Res.*, **92**, 4639–4648, 1987.

Nakajima, H., S. Okano, H. Fujinishi, and T. Ono, Observations of thermospheric wind velocities and temperatures by the use of a Fabry-Perot Doppler imaging system at Syowa Station, Antarctica, *Appl. Opt.*, **34**, 8382–8395, 1995.

Price, G. D., R. W. Smith, and G. Hernandez, Simultaneous measurements of large vertical winds in the upper and lower thermosphere, *J. Atmos. Terr. Phys.*, **53**, 631–643, 1995.

Rees, M. H. and J. C. G. Walker, Ion and electron heating by auroral electric fields, *Ann. Geophys.*, **24**, 193–199, 1968.

Rees, M. H., B. A. Emery, R. G. Roble, and K. Stamnes, Neutral and ion gas heating by auroral electron precipitation, *J. Geophys. Res.*, **88**, 6289–6300, 1983.

Rees, D., R. W. Smith, P. J. Charleton, F. G. McCormac, N. Lloyd, and Å. Steen, The generation of vertical thermospheric winds and gravity waves at auroral latitudes—I. Observations of vertical winds, *Planet. Space Sci.*, **32**, 667–684, 1984.

Roble, R. G. and M. H. Rees, Time-dependent studies of the aurora: Effects of particle precipitation on the dynamic morphology of ionospheric and atmospheric properties, *Planet. Space Sci.*, **25**, 991–1010, 1977.

Sahai, Y., J. A. Bittencourt, H. Takahashi, and M. Mendillo, Comparison of a low-latitude ionospheric model with observations of OI 630 nm emission and ionospheric parameters, *Planet. Space Sci.*, **38**, 1243–1250, 1990.

Sato, T., Radar principles, *International School on Atmospheric Radar Lecture Notes*, edited by S. Fukao, Kyoto, 417 pp., Nov. 24–28, 1988.

Shepherd, G. G., G. Thuillier, B. H. Sollheim, Y. J. Rochon, J. Criswick, W. A. Gault, R. N. Peterson, R. H. Wiens, and S.-P. Zhang, WINDII on UARS—Status report and preliminary results, The upper mesosphere and lower thermosphere: a review of experiment and theory, *Geophys. Mono.*, **87**, 297–304, American Geophysical Union, 1995.

Smith, R. W. and G. Hernandez, Vertical winds in the thermosphere within the polar cap, *J. Atmos. Terr. Phys.*, **53**, 611–620, 1995.

Vallance Jones, A., R. L. Gattinger, F. Creutzberg, F. R. Harris, A. G. McNamara, A. W. Yau, E. J. Llewellyn, D. Lummerzheim, M. H. Rees, I. C. McDade, and J. Margot, The Aries auroral modelling campaign: Characterization and modelling of an evening auroral arc observed from a rocket and a ground-based line of meridian scanners, *Planet. Space Sci.*, **39**, 1677–1705, 1991.

Walterscheid, R. L., L. R. Lyons, and K. E. Taylor, The perturbed neutral circulation in the vicinity of a symmetric stable auroral arc, *J. Geophys. Res.*, **90**, 12235–12248, 1985.

Wickwar, V. B., J. W. Meriwether, Jr., P. B. Hays, and A. F. Nagy, The meridional thermospheric neutral wind measured by radar and optical techniques in the auroral region, *J. Geophys. Res.*, **89**, 10987–10998, 1984.

M. Ishii (e-mail: mishii@crl.go.jp), S. Oyama, S. Nozawa, R. Fujii, E. Sagawa, S. Watari, and H. Shinagawa